



University of
Zurich^{UZH}

Zurich Open Repository and
Archive

University of Zurich
University Library
Strickhofstrasse 39
CH-8057 Zurich
www.zora.uzh.ch

Year: 2022

Broadband Model-Based Optoacoustic Mesoscopy Enables Deep-Tissue Imaging beyond the Acoustic Diffraction Limit

Li, Weiye ; Hofmann, Urs A T ; Rebling, Johannes ; Zhou, Quanyu ; Chen, Zhenyue ; Ozbek, Ali ; Gong, Yuxiang ; Subochev, Pavel ; Razansky, Daniel ; Deán-Ben, Xosé Luís

Abstract: Optoacoustic mesoscopy (OAM) retrieves anatomical and functional contrast in vivo at depths not resolvable with optical microscopy. Recent progress on reconstruction algorithms have further advanced its imaging performance to provide high lateral resolution ultimately limited by acoustic diffraction. In this work, a new broadband model-based OAM (MB-OAM) framework efficiently exploiting scanning symmetries for an enhanced performance is presented. By capitalizing on the large detection bandwidth of a spherical polyvinylidene difluoride film while accurately accounting for its spatial impulse response, the new approach significantly outperforms standard OAM implementations in terms of contrast and resolution, as validated by functional in vivo experiments in mice and human volunteers. Furthermore, L1-norm regularization enables resolving structures separated by less than the theoretical diffraction-limited resolution. This unique label-free angiographic performance demonstrates the general applicability of MB-OAM as a super-resolution deep-tissue imaging method capable of breaking through the limits imposed by acoustic diffraction.

DOI: <https://doi.org/10.1002/lpor.202100381>

Posted at the Zurich Open Repository and Archive, University of Zurich

ZORA URL: <https://doi.org/10.5167/uzh-231767>

Journal Article

Published Version



The following work is licensed under a Creative Commons: Attribution 4.0 International (CC BY 4.0) License.

Originally published at:

Li, Weiye; Hofmann, Urs A T; Rebling, Johannes; Zhou, Quanyu; Chen, Zhenyue; Ozbek, Ali; Gong, Yuxiang; Subochev, Pavel; Razansky, Daniel; Deán-Ben, Xosé Luís (2022). Broadband Model-Based Optoacoustic Mesoscopy Enables Deep-Tissue Imaging beyond the Acoustic Diffraction Limit. *Laser and Photonics Reviews*, 16(5):2100381. DOI: <https://doi.org/10.1002/lpor.202100381>

Broadband Model-Based Optoacoustic Mesoscopy Enables Deep-Tissue Imaging beyond the Acoustic Diffraction Limit

Weiye Li, Urs A. T. Hofmann, Johannes Rebling, Quanyu Zhou, Zhenyue Chen, Ali Ozbek, Yuxiang Gong, Pavel Subochev, Daniel Razansky, and Xosé Luís Deán-Ben*

Optoacoustic mesoscopy (OAM) retrieves anatomical and functional contrast in vivo at depths not resolvable with optical microscopy. Recent progress on reconstruction algorithms have further advanced its imaging performance to provide high lateral resolution ultimately limited by acoustic diffraction. In this work, a new broadband model-based OAM (MB-OAM) framework efficiently exploiting scanning symmetries for an enhanced performance is presented. By capitalizing on the large detection bandwidth of a spherical polyvinylidene difluoride film while accurately accounting for its spatial impulse response, the new approach significantly outperforms standard OAM implementations in terms of contrast and resolution, as validated by functional in vivo experiments in mice and human volunteers. Furthermore, L1-norm regularization enables resolving structures separated by less than the theoretical diffraction-limited resolution. This unique label-free angiographic performance demonstrates the general applicability of MB-OAM as a super-resolution deep-tissue imaging method capable of breaking through the limits imposed by acoustic diffraction.

in this depth range, thus are generally tailored for the biomedical application of interest.^[1,2] For example, OA tomography based on concave piezoelectric arrays has been shown to capitalize on a large angular coverage to render accurate images of arbitrarily oriented vascular networks.^[3,4,5] However, although tomographic high-resolution imaging has been enabled with high-frequency arrays,^[6] deep-tissue OA mesoscopy (OAM) is typically performed by raster-scanning a single-element transducer.^[7,8,9,10,11,12] This approach represents one of the most common OA embodiments and is increasingly being used in preclinical and clinical studies requiring high-resolution imaging.^[13,14] Alternatively, OA tomography can image deeper tissue layers at inferior spatial resolutions by detecting low frequency US waves in real time using sensor


1. Introduction

Advanced acoustic inversion methods are essential to optimize the achievable resolution, contrast, and overall performance of optoacoustic (OA, photoacoustic) imaging systems operating at depths not resolvable with optical microscopy (>1 mm in biological tissues). The type and location of ultrasound (US) sensor(s) mainly determine the imaging performance

arrays, which is preferred in some clinical applications.^[15,16] An important advantage of OAM over tomographic OA methods is a significantly simpler and less expensive instrumentation. More importantly, OAM is particularly suitable for exploiting the multiscale OA imaging capabilities by covering an otherwise unachievable signal bandwidth. For example, centimeter-scale depths have been achieved with transducers featuring detection bandwidths of a few MHz,^[7,17] while ultra-wideband detectors have been used, e.g., in raster-scan OA mesoscopy, an implementation of OAM, for high-resolution imaging at depths around 2 mm – 4 mm.^[13,18] Multiple scales can additionally be covered simultaneously, e.g., via coaxial light focusing in hybrid-focus OAM^[19,20] or with a dual-element transducer in quad-mode OAM.^[21]

The importance of OAM fostered ongoing efforts on the optimization of image formation methods. The synthetic aperture focusing technique (SAFT), also used in radar, sonar, and biomedical US, has become the standard image formation method in OAM.^[10] SAFT was introduced in OAM as the virtual detector concept,^[22] and is generally implemented using the delay-and-sum (DAS) technique in the time domain.^[23] More advanced approaches based on weighting factors in the time or frequency domains^[24,25] or on delay-multiply-and-sum methods^[26,27] have further been shown to provide an enhanced performance. DAS can be regarded as a discrete implementation of the filtered back-projection algorithm, derived from the time-domain

W. Li, U. A. T. Hofmann, J. Rebling, Q. Zhou, Z. Chen, A. Ozbek, Y. Gong, D. Razansky, X. L. Deán-Ben
Institute for Biomedical Engineering and Institute of Pharmacology and Toxicology
University of Zurich and ETH Zurich
Zurich 8057, Switzerland
E-mail: xl.deanben@pharma.uzh.ch
P. Subochev
Institute of Applied Physics
Russian Academy of Sciences
Nizhny Novgorod 603600, Russia

 The ORCID identification number(s) for the author(s) of this article can be found under <https://doi.org/10.1002/lpor.202100381>

© 2022 The Authors. Laser & Photonics Reviews published by Wiley-VCH GmbH. This is an open access article under the terms of the Creative Commons Attribution License, which permits use, distribution and reproduction in any medium, provided the original work is properly cited.

DOI: 10.1002/lpor.202100381

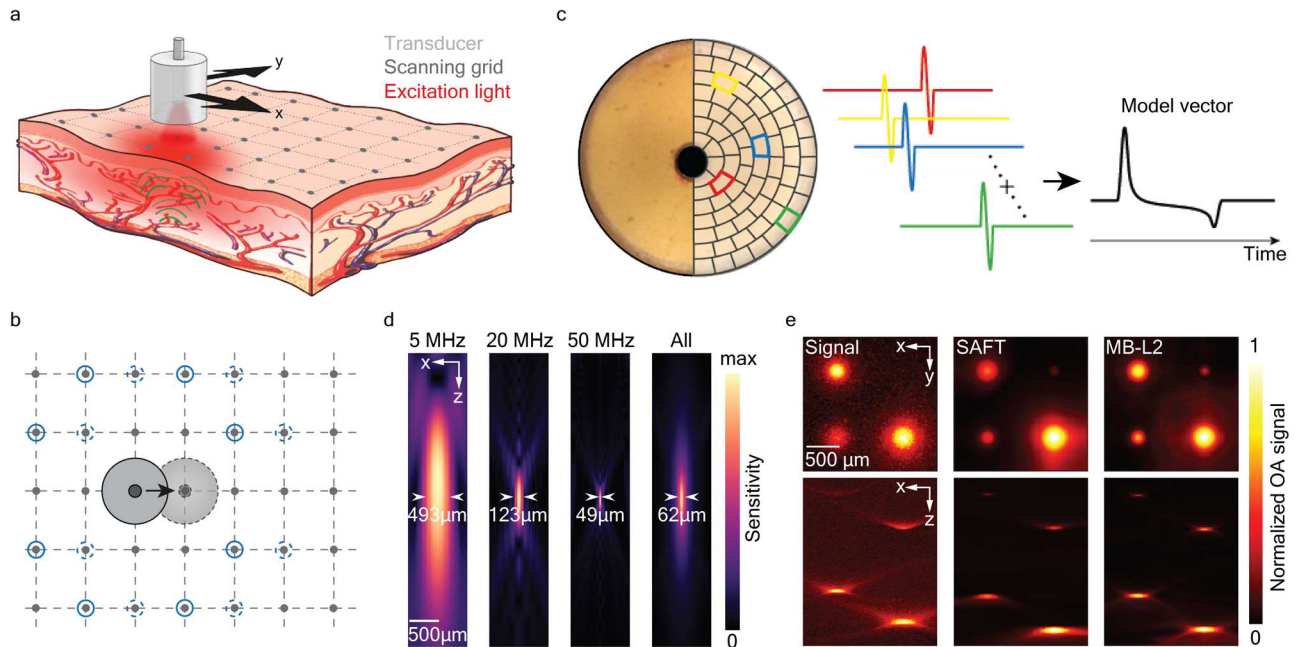


Figure 1. Time-domain model for OAM. a) Raster-scan image acquisition protocol. b) Schematic representation of the scanning symmetries. The OA signals generated at all voxels labeled with blue circles for the indicated transducer position are equivalent. Signals are preserved if the transducer and voxels are shifted by the same distance (dashed lines). c) Photograph of the sensing area of transducer (left), and a representation of the OA model based on discretizing transducer surface into sub-elements (right). The OA signals corresponding to a given voxel and all surface elements are superimposed to estimate the collected time-resolved signal for that voxel. d) Cross-sectional view of the amplitude spectral density of the modeled time-resolved signals for three different frequencies along with amplitude of these signals in the time domain. FWHM values are indicated. e) OAM images reconstructed by superimposing the acquired signals (left), with the SAFT method (middle) and with the MB-L2 method (right).

OA forward model for short-pulsed excitation.^[28] Such a model represents a solid mathematical foundation enabling the development of more accurate acoustic inversion methods. Thus, algorithms based on time reversal techniques,^[29,30] model-based (MB) iterative inversion algorithms^[31,32,33] or hybrid-domain modeling of a focused transducer^[30] have been suggested for OAM. MB inversion in the time domain is arguably the most accurate approach to account for the finite size and shape of US sensors.^[34,35,36] Additionally, the performance of iterative inversion can be enhanced by properly choosing constraints or regularization terms.^[37,38,39,40,41,42] However, implementation of this method for the dense grid of voxels required for high-resolution volumetric imaging has remained challenging due to extremely high computational costs, even when considering efficient parallel implementations in graphics processing units (GPUs).^[43,44]

Herein, we introduce a new broadband MB-OAM image formation framework that efficiently exploits scanning symmetries to enable GPU-based, high-resolution, volumetric imaging. The underlying time-domain OA forward model accurately accounts for the large bandwidth of the OA signals collected with a custom-made spherical polyvinylidene difluoride (PVDF) transducer, while discretization of the transducer surface additionally enables modeling its spatial impulse response (SIR). MB inversion is shown to significantly enhance the achievable resolution even beyond the acoustic diffraction limit, thus outperforming standard OAM implementations as well as other optical modalities based on extrinsically administered contrast agents. The label-free nature of OA ensures that the suggested approach is generally applicable in any preclinical or clinical application re-

quiring visualization of tissues at depths not reachable with optical microscopy.

2. Results

2.1. Accurate Modeling of OA Signals

OAM acquires volumetric images in a raster-scanning acquisition protocol (Figure 1a and Figure S1, Supporting Information) with spatial sampling (scanning step) fulfilling the Nyquist criterion. The lateral resolution in OAM is considered to be limited by acoustic diffraction to $0.71\lambda/NA$,^[45] where λ and NA are the central wavelength and numerical aperture of the US transducer. Typical lateral resolutions are in the range of $40\ \mu\text{m}$, for which scanning steps around a few tens of micrometers are needed. The suggested MB-OAM defines time-resolved OA signals corresponding to each pair of voxel and scanning position, where the lateral positions of the voxels match the x-y scanning positions (see Experimental Section for details). For a raster-scan configuration, the OA model is translational-symmetric — signals are identical if the relative position between the voxel and scanning point is maintained (Figure 1b). A spherical US transducer further defines axial symmetries with respect to the acoustic axis (Figure 1b). Accurate modeling of the impulse response of the transducer is achieved by splitting it into two terms, namely the electrical impulse response (EIR) defining the effective detection bandwidth, and the SIR accounting for acoustic diffraction effects associated to the finite size of the sensing area.^[46] A custom-made transducer consisting of a PVDF film

featuring broad detection bandwidth (~ 1 MHz – 100 MHz) was used herein^[11] (Figure 1c, see Experimental Section for details). Note that the sensitivity of the transducer decreases at frequencies beyond 50 MHz (Figure S2, Supporting Information) and frequency dependent attenuation further low-pass filters US waves propagating through tissues and coupling medium. Thereby, the achievable contrast-to-noise ratio of the images reconstructed by filtering the signals within the frequency range of 50 MHz – 100 MHz is very low (Figure S2, Supporting Information). The spatially dependent SIR of the spherically focused, axially symmetric transducer strongly limits the lateral resolution at planes distant from the focal plane,^[22] and standard image formation methods (SAFT and its variants) cannot fully compensate for this effect. In the suggested MB framework, the SIR for each voxel was estimated by superimposing the corresponding time-resolved OA signals for a set of surface elements (e.g., 1000) covering the active sensing area (Figure 1c). This is equivalent to adding up the OA forward model corresponding to each surface element (see Experimental Section for details). Considering the scanning symmetries, the information in the model-matrix is fully contained in the sub-matrix corresponding to an individual scanning point, thus could be stored in the memory of state-of-the-art GPUs (1.3 GB for half a million voxels and 837 time points, see Experimental Section for details). The memory required to store the OA forward model is invariant to the arbitrarily large lateral dimensions of the scan area, which allows storing the OA signals, the model, and the reconstructed absorber distribution simultaneously on a GPU. Thereby, large volumetric images can be reconstructed at high-resolution in a reasonable time. A detailed overview of reconstruction times as a function of scanning area and step size is provided in Table S1 (Supporting Information). The amplitude spectral density of the time-domain OA forward model (columns of the model matrix) reveals the expected diffraction patterns at different frequencies, while their amplitude in the time domain defines the sensitivity field of a transducer matching the expected diffraction-limited resolution for broadband OA signals (Figure 1d). The capability to encode frequency-dependent information empowers the suggested MB framework with unique capabilities to reconstruct absorbers with different sizes emitting OA waves in different frequency bands, clearly outperforming alternative approaches, e.g., based on superimposing signals or SAFT (Figure 1e).

2.2. Imaging beyond the Acoustic Diffraction Barrier

Mathematically, MB inversion minimizes an energy functional consisting of a data fidelity term driving the solution towards the observed data, and a regularization term that stabilizes the inversion and includes prior information.^[47] OAM image formation is challenged by the limited-view scanning geometry and the associated ill-posed nature of the inverse problem.^[48] Regularization hence turns essential for computing a credible approximation of the light absorption distribution. Tikhonov regularization, based on the L2 norm, is the classical method for noise-robust inversion and represents the most probable solution given the raw signals and a prior Gaussian distribution of measurement noise. The MB algorithm based on an L2 regularization term (MB-L2, see Experimental Section for details) enabled enhancing the lateral

resolution and contrast of OAM images at out-of-focus locations beyond SAFT (Figure 1e). However, reconstruction of closely separated (at a distance of 40 μm), simulated absorbers at the focal plane indicate that the lateral resolution is still limited by acoustic diffraction (Figure 2a,b). This is expected considering that MB-L2 is a linear inversion procedure equivalent to time-reversed propagation of US waves.^[49] Alternatively, regularization terms based on the L1 norm can be used to promote sparse solutions in a given domain. Particularly, an L1-based regularization term in the image domain tends to set many voxels to zero (or close to zero) values. Simulation results with relatively separated absorbers indicated that the full width at half maximum (FWHM) of the absorbers reconstructed with the MB algorithm with L1 regularization (MB-L1, see Experimental Section for details) is considerably smaller (13 μm) than the FWHM achieved with SAFT (43 μm) and MB-L2 (41 μm , Figure 2a,b). This could be erroneously interpreted as a narrower point spread function (PSF) of the imaging system enabling higher resolution. However, MB-L1 is a non-linear inversion procedure and hence a PSF cannot be defined. Instead, the achievable resolution must be estimated from the reconstructed image of closely separated sources. In this regard, undistinguishable absorbers in the images obtained with SAFT and MB-L2 could be separated with MB-L1, thus effectively breaking through the acoustic diffraction barrier (Figure 2a,b and Figure S3, Supporting Information). Simulation results with more sophisticated structures mimicking vascular networks further corroborated the super-resolution imaging performance of MB-L1 (Figure S4, Supporting Information). The effect of the EIR was estimated by filtering the simulated signals corresponding to a 20 μm absorber with different cut-off frequencies (Figure S5, Supporting Information). The size of the reconstructed absorber does not significantly change for signal bandwidths above 40 MHz to 50 MHz, while it deviates significantly for signal bandwidths below 20 MHz. Super-resolution methods based on processing a sequence of low resolution images have long been developed. The L1 norm has been used in the data fidelity term to achieve optimal regularized inversion in the presence of noise.^[50] Regularization based on the L1 norm has also been used for an enhanced performance when prior information on image sparsity is available,^[51] even for single-image super-resolution.^[52] Similarly, L1-based regularization has also been used for super-resolution biomedical image reconstruction.^[53,54] Note, however, that sparsity in biomedical images may be expressed in different domains depending on specific features of each modality.

Experimental results with an agar phantom embedding a microsphere with 20 μm diameter slightly out-of-focus corroborated the simulation results (Figure 2c,d, see Experimental Section for details). The OA signals and forward model were band-pass filtered between 0.5 MHz and 80.0 MHz, yielding an effective diffraction limit of 61 μm (see Experimental Section for details). The FWHM of the reconstructed sphere was significantly reduced with MB-L1 compared to SAFT and MB-L2, while it was also possible to distinguish two closely separated spheres simulated by shifting the scanning position and adding up the corresponding OA signals (Figure 2c,d, see Experimental Section for details). Additional experiments with an agar phantom embedding carbon fibers with 7 μm diameter further validated the enhanced resolution achieved with MB-L1 (Figure 2e,f). The width

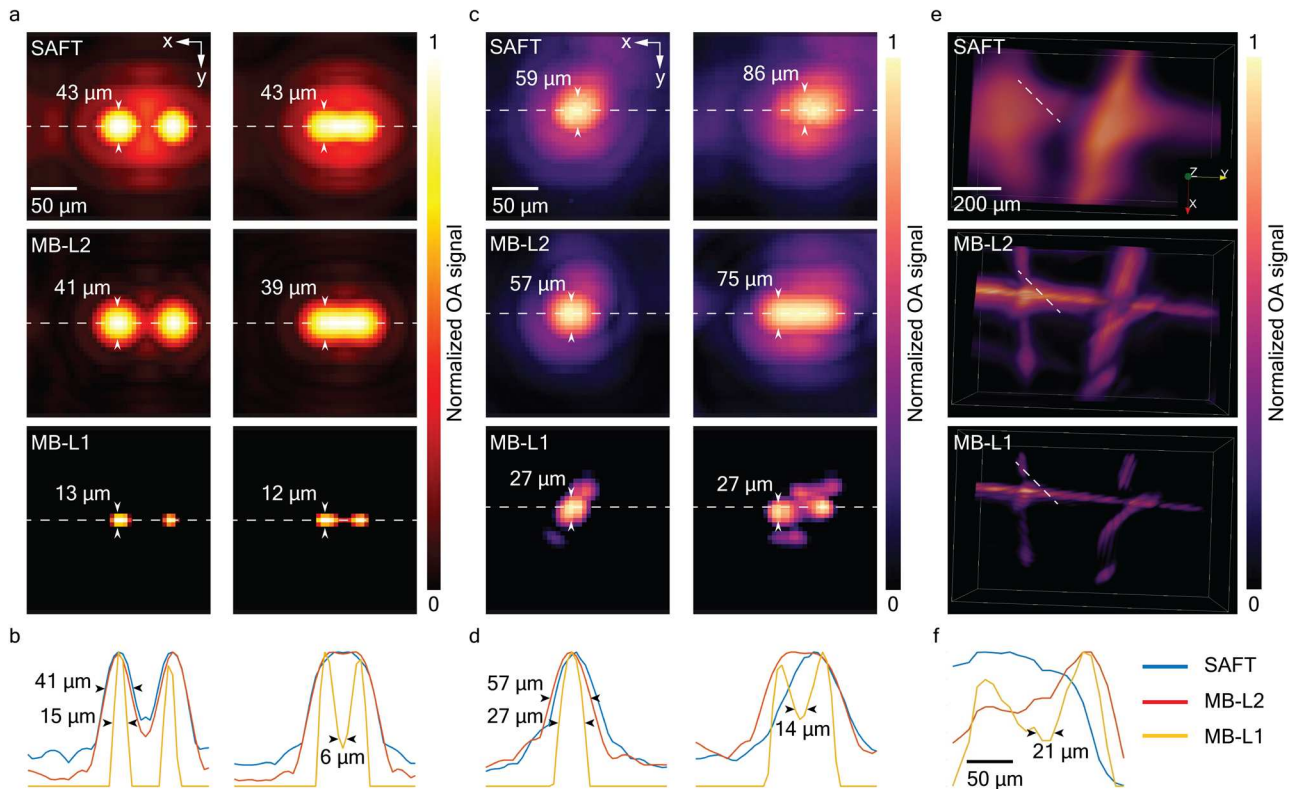


Figure 2. Super-resolution imaging beyond the acoustic diffraction limit. a) MIPs of the OAM images reconstructed with the SAFT (top), MB-L2 (middle) and MB-L1 (bottom) methods from simulated data corresponding to two 20 μm absorbers separated by 60 μm (left) and 40 μm (right). FWHM are indicated. b) Cross-sectional profiles for the dashed lines indicated in (a). FWHM are indicated in the left panel, and separation for points >20% of the minimum is indicated in the right panel. c) MIPs of the OAM images reconstructed with the SAFT (top), MB-L2 (middle), and MB-L1 (bottom) methods from experimental data corresponding to a 20 μm sphere. Reconstructions from the original time-resolved signals and from the superposition of signals shifted by 40 μm are shown (left and right respectively). FWHM are indicated in the left panel and separation for points >20% of the minimum is indicated in the right panel. d) Cross-sectional profiles for the dashed lines indicated in (c). FWHM are indicated in the left panel and separation for points >20% of the minimum is indicated in the right panel. e) MIPs of the OAM images reconstructed with the SAFT (top), MB-L2 (middle) and MB-L1 (bottom) methods from experimental data corresponding to 7 μm carbon fibers. f) Cross-sectional profiles for the dashed lines indicated in (e). Separation for points >20% of the minimum is indicated.

of the reconstructed fibers was significantly reduced with MB-L1. More importantly, MB-L1 enabled resolving crossing fibers at points where SAFT and MB-L2 failed (Figure 2f). Note that the resolution achieved with MB-L2 by taking the high frequency components (50 MHz – 100 MHz) of the signals could not surpass the resolution achieved with MB-L1 (Figure S6, Supporting Information).

2.3. Enhanced Angiographic Imaging In Vivo

The accuracy of the OA forward model turns essential for precise reconstruction of more complex structures in living organisms. Proper selection of the regularization term is also highly important. Most commonly, OA visualizes multi-scale vascular networks in space or frequency domains, which poses challenges on defining a priori information on the images. However, considering that OAM images mainly visualizes vascular networks at scales covered by the detection bandwidth of the transducer, it is reasonable to assume a certain sparsity degree in the image domain. A raster-scan with 25 μm step size across the back of a

CD-1 mouse (Figure 3a, see Experimental Section for details) enabled comparing the in vivo imaging performance of different image formation approaches. SAFT, MB-L2, and MB-L1 successfully visualized microvascular structures in this region, although clear differences were observed in image quality and content (Figure 3b). A smoothing effect was observed in the blood vessels reconstructed with SAFT, which degrades the achieved resolution. The vascular network at different depths is clearly better resolved in the MB-L2 image, including branches not visible with SAFT. The sharpening effect of MB-L1 compared to MB-L2 was similar to the observations in simulation and phantom experiments. The width of the reconstructed vessels is clearly narrowed compared to the other two approaches. However, MB-L1 appears to reduce the available information in the image. Many of the branches visible in the MB-L2 image are not seen with MB-L1, arguably due to the sparsity constraint, i.e., MB-L1 tends to set voxels actually corresponding to vessels to zero. This represents a limitation of the MB-L1 approach in practical cases, particularly when the sparsity of the vascular networks covered by the OAM system is relatively low. The achieved resolution with different approaches can be more clearly compared in a three-dimensional view of the central part of the scan (Figure 3c). Individual vessels and branches in

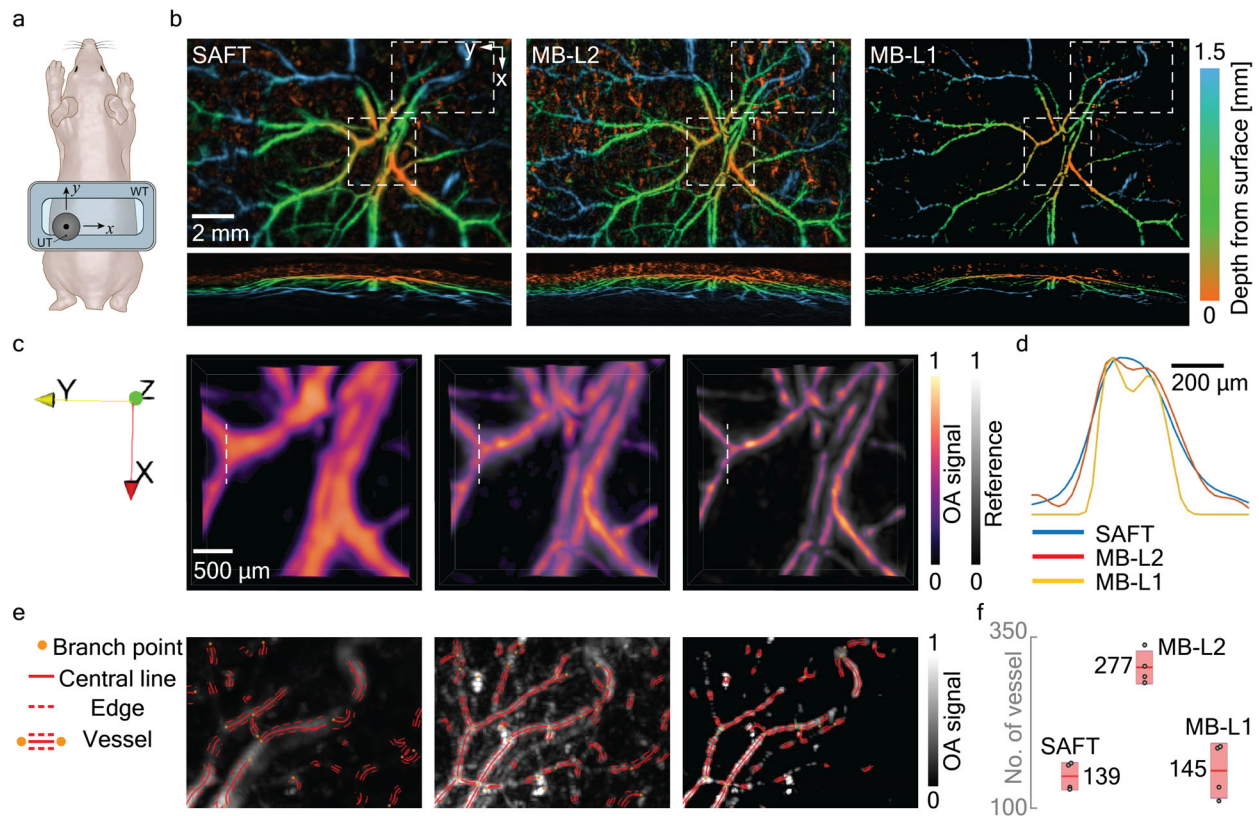


Figure 3. Enhanced angiographic imaging capabilities. a) Lay-out of the in vivo imaging scheme indicating the scanned region. b) Depth color-encoded MIPs of the OAM images reconstructed with the SAFT (left), MB-L2 (middle), and MB-L1 (right) methods. c) Three-dimensional views of the central region indicated in (b). The reference images are the SAFT image in the middle panel and the MB-L2 image in the right panel. d) Cross-sectional profiles indicated in (c). e) Reconstructed vessels in the binarized image corresponding to the indicated region in the upper right corner in (b). f) Number of detected vessels for four different in vivo datasets reconstructed with SAFT, MB-L2, and MB-L1. The average number of vessels is indicated for each reconstruction method.

MB-L1 and MB-L2 images are shown to be more clearly defined than in superimposed MB-L2 and SAFT images, respectively. Coherent factor weighting can be used to enhance contrast and spatial resolution in SAFT.^[22] However, the observed performance of this approach was still lower than that of MB-L2 and MB-L1 (Figure S7, Supporting Information). A comparison of the image profiles for a region close to a branching point corroborates that MB-L1 can break through the resolution limit of SAFT and MB-L2 (Figure 3d). Note that the selected profile could not be better resolved with MB-L2 taking the high frequency components (50 MHz – 100 MHz) of the signals or when combining images reconstructed with different bandwidths (Figure S6, Supporting Information). The image content was better assessed by quantifying the amount of vessels in the binarized images with an automatic vessel segmentation and analysis (AVSA) algorithm^[55] (Figure 3e, see Experimental Section for details). Statistical analysis of the number of detected vessels from four different mouse back datasets showed that, on average, the number of vessels in the MB-L2 image is higher by almost twofold with respect to SAFT and MB-L1 images (Figure 3f). Overall, the suggested MB image formation framework significantly enhanced the performance of SAFT in vivo, while the regularization choice establishes a trade-off between achievable resolution and visibility of vascular networks.

2.4. Toward Quantitative Clinical Imaging

Microvascular alterations are involved in many physiological and pathophysiological processes and serve as indicators of diabetes, cancer, neurological disorders, and other human diseases. The powerful microvascular imaging capabilities of the suggested MB-OAM are best appreciated when validating the images obtained against those rendered with established angiographic methods (Figure 4a). A bright field image of a region in the back of a nude-Fox1nu mouse enables identifying superficial blood vessels in the skin. Vascular contrast and imaging depth can be enhanced, e.g., via injection of indocyanine green (ICG), a water-soluble dye routinely used in the clinics that fluoresces in the near infrared (NIR-I, ≈ 650 nm – 1000 nm) window of light. Recently, the availability of cameras sensitive to photons in the second near-infrared (NIR-II, ≈ 1000 nm – 1700 nm) window featuring reduced light scattering and autofluorescence has enabled reaching depths previously unattainable with optical methods. The vascular structures observed in the fluorescence images are also visible in the image obtained with MB-L2, which additionally enables visualizing smaller and deeper vessels with endogenous contrast (Figure 4a).

The capability of the suggested approach to quantify microvascular changes was further tested by assessing responses to

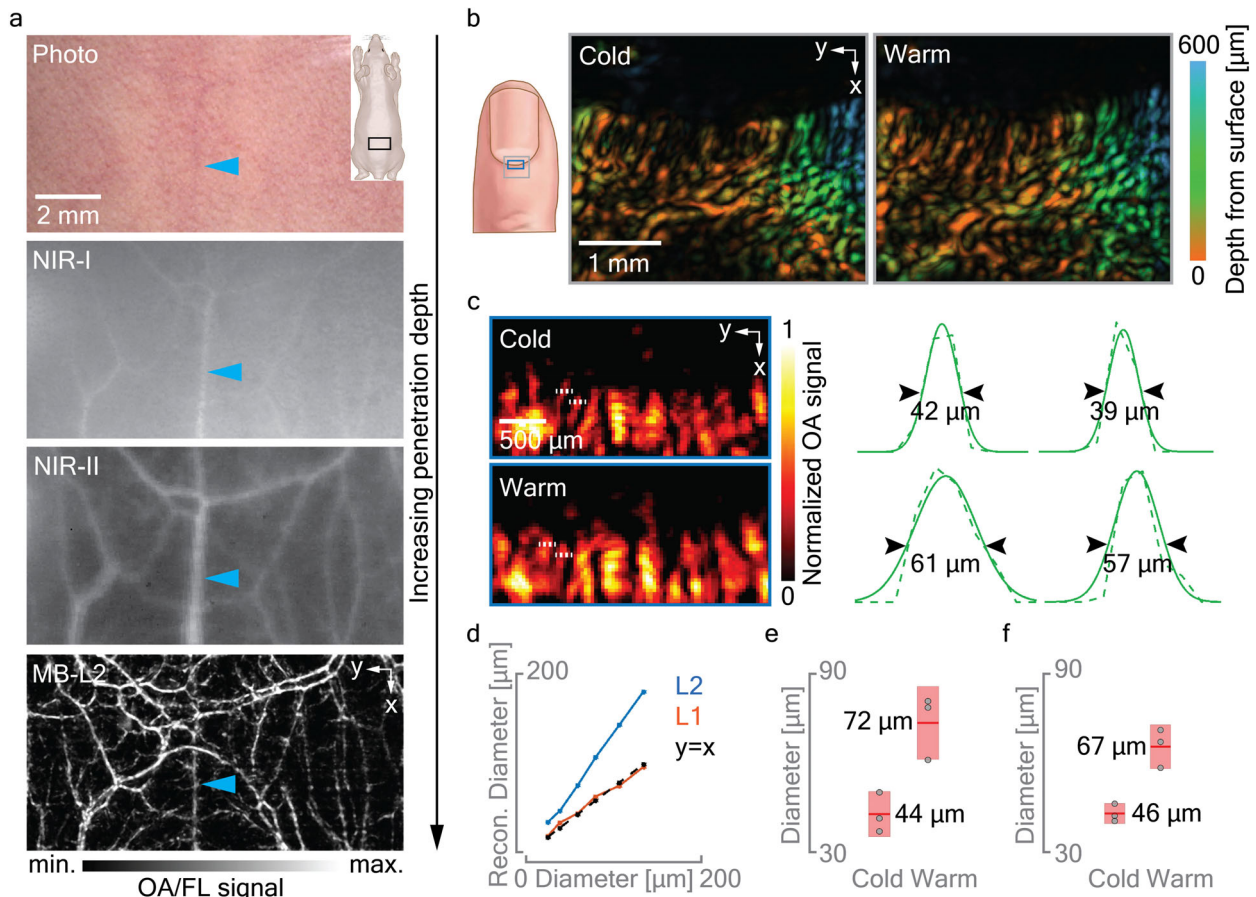


Figure 4. Validation and quantification of microvascular changes. a) Comparison of OAM with established angiographic imaging approaches. From top to bottom — bright field optical imaging, NIR-I fluorescence image following injection of ICG, NIR-II fluorescence image following injection of ICG, OAM image reconstructed with MB-L2. The imaged region in the mouse is indicated. Cyan arrowheads indicate a vertical vessel present in all four modalities. b) OAM images (reconstructed with MB-L2) of the cuticle vasculature of a healthy volunteer following immersion in cold and warm water. The imaged region in the finger is indicated. c) OAM images (reconstructed with MB-L1) of the nailfold arterioles and venules. The imaged region in the finger is indicated. The indicated profiles and fitted Gaussian curves are also shown. d) Reconstructed diameter of a simulated sphere as a function of the actual diameter for MB-L1 and MB-L2. The line corresponding to ideal reconstruction ($y = x$) is indicated. e) Measured diameters (FWHMs in the MB-L1 images) of 3 microvessels in a volunteer following immersion in cold and warm water. f) Average of measured diameters (FWHMs in the MB-L1 images) in $n = 3$ healthy volunteers following immersion in cold and warm water.

thermal stimuli in images of the cuticle microvasculature of healthy volunteers (see Experimental Section for details). MB-L2 images acquired after exposure to cold and warm water revealed a higher vascular density in the second case (Figure 4b). Qualitative image quality may further be enhanced via post-processing, e.g., with a Frangi filter, which may however lead to the appearance of inexistent vessels in the images (Figure S8, Supporting Information). Considering that the tissue temperature is expected to be approximately the same at the measuring time points, these differences are ascribed to thermally induced microvascular alterations. Quantification of vasodilation was better achieved in MB-L1 images of the nailfold region (Figure 4c). Numerical simulations considering spheres with different sizes (see Experimental Section for details) indicate that MB-L1 provides more accurate dimensional readings than MB-L2 (Figure 4d, Figure S9, Supporting Information). MB-L1 further capitalizes on the relative sparsity of the images of this area to better resolve arterioles and venules. Consistent results on relative vasodilation were ob-

tained for different vessels of the same volunteer (Figure 4e) and across different volunteers (Figure 4f), which indicates the general applicability of MB-L1 for assessing microvascular changes.

The deep-tissue imaging capability of the suggested approach was further demonstrated by considering the wrist of a healthy volunteer at 532 nm and 1064 nm wavelengths (Figure S10, Supporting Information). In this region, both superficial vessels (as shallow as 0.12 mm from the skin surface) and deep-seated vessels (up to 1.34 mm from the skin surface) were resolved with MB-L2 and MB-L1 when 532 nm was used as excitation wavelength, while no deep-seated vessels were observed in the images reconstructed with SAFT (Figure S10, Supporting Information). This depth regime is not reachable with optical-resolution OAM. Line profiles from vessels located at around 0.8 mm below the skin surface further demonstrated the enhanced resolution achieved with MB-L1 with respect to SAFT and MB-L2. At 1064 nm excitation wavelength, light attenuation is significantly reduced. This, in principle, facilitates

deep-tissue imaging. However, vascular contrast decreases at this near-infrared wavelength due to low absorption of light, and only large vessels were clearly visible in the SAFT, MB-L2 and MB-L1 reconstructed images (Figure S10, Supporting Information). Compared to SAFT, the proposed MB-L2 and MB-L1 methods visualized large, deep-seated vessels (beyond 1 mm from the skin surface) with better contrast. The line profiles also demonstrated spatial resolution improvement of MB-L1 over MB-L2 and SAFT. Note, however, that resolution enhancement is more relevant for small microvessels, which were not clearly visible in the images taken at 1064 nm wavelength. Thereby, the trade-off between image contrast and attenuation associated to light absorption at a given wavelength is an essential factor to establish the achievable high-resolution imaging depth in practical cases.

3. Discussion and Conclusion

Numerical simulations as well as phantom and in vivo experiments demonstrated the enhanced performance of the suggested MB-OAM framework with respect to standard OAM. This is in agreement with what has been shown in several OA tomographic configurations.^[40,56,57,58] However, OAM aims at a significantly higher resolution than OA tomography combined with large field-of-view (FOV). The implementation of volumetric MB iterative inversion methods is thereby significantly challenged by the fact that the full model matrix, corresponding to the linear operator mapping the initial pressure distribution (OA image) into measured pressure signals, becomes too large to be stored in GPU or even CPU memory. By exploiting the translational and axial symmetries of the model for the spherically focused transducer within the scanning plane and its limited lateral sensitivity, the model matrix was effectively “compressed” into a sub-matrix corresponding to a single scanning position and the voxel grids sufficiently close to it. The size of this sub-matrix is defined by the lateral sensitivity, the desired imaging depth, and the number of time instances, i.e., it is invariant with respect to an arbitrarily large reconstruction grid. Therefore, the suggested MB reconstruction framework is expected to be generally applicable in any OAM system. The advantages of MB inversion stem from the fact that it accurately accounts for the broadband nature of OA signals. This is fundamentally different to other approaches considering an approximation of the transducer sensitivity field, which generally changes for different OA sources due to the frequency dependence of the diffraction-limited acoustic focusing. In the current implementation, the model matrix was estimated theoretically by integrating the acoustic pressure distribution at the surface of the transducer, which represents a valid approximation for the curved thin PVDF film employed. However, the theoretical computation of the model matrix, e.g., for transducers based on acoustic lenses or air-coupled transducers is more complex as it involves modeling acoustic interfaces.^[59,60] The suggested reconstruction methodology can alternatively be used by experimentally estimating the model matrix for a transducer position, e.g., by raster-scanning a small particle or a light beam in the volume of interest.^[61] Other parameters can also be considered in the model, such as the light fluence distribution or acoustic attenuation effects, which may lead to further improvements in quantification and spatial resolution.^[62,63]

Acoustic diffraction has been considered as a limit for the achievable resolution in OA, similar to light diffraction in optical microscopy.^[64] Super-resolution methods have massively impacted life sciences by smartly overcoming the optical diffraction limit.^[65] The development of similar approaches enabling breaking through the acoustic diffraction barrier at depths not reachable with optical microscopy is also expected to highly influence the biomedical imaging field and boost the applicability of OA as a research and clinical tool. Well-established optical super-resolution methods can be taken as a reference for this purpose, although fundamental differences exist in physical principles and instrumentation. Recently, localization OA tomography exploited the basic principle of photoactivated localization microscopy to image beyond the resolution limit imposed by acoustic diffraction.^[9,66,67,68,69] The super-resolution method suggested herein (MB-L1) has some analogies with stimulated emission depletion microscopy as it is based on a raster-scan protocol where a non-linear response is induced. The non-linearity is however associated with the reconstruction procedure, hence MB-L1 also has similarities with super-resolution methods based on multiple observations with sub-pixel displacements and/or sparse image representations.^[52,70] Regularization terms based on the L1 norm have been used for OA tomographic reconstruction of relatively sparse objects since early developments in MB algorithms.^[71] This approach was then used in several algorithms to exploit the sparse nature of the OA images of vascular networks.^[58,72] Image sparsity in other domains has also been considered.^[38,73] Total variation regularization, also based on the L1 norm, is also widely used in OA reconstructions,^[74] which was further adapted, e.g., to account for complex-nonconvex structures^[75] or to simultaneously consider spatial and temporal information.^[42] L1-based regularization has been shown to reduce the width of reconstructed structures in phantom experiments performed with OA tomography.^[76,77] Herein, we have further demonstrated that the suggested OA forward model is sufficiently accurate to better resolve closely separated sources — branching vascular structures — in vivo, which effectively demonstrates its performance as a super-resolution biomedical imaging tool. MB-L1 was further shown to provide accurate dimensional readings that can be exploited for the quantification of vasodilation or other microvascular alterations associated to human diseases.

The enhanced spatial resolution and overall imaging performance provided by the proposed MB-OAM framework is expected to expand the use of OAM in preclinical and clinical applications, particularly in those requiring high-resolution imaging at depths not reachable with optical microscopy. OAM enables bridging the gap between microscopic and macroscopic imaging modalities to cover an otherwise inaccessible mesoscopic imaging range. An excellent review of emerging applications of OA mesoscopy is available.^[78] To name a few examples, OAM has enabled label-free visualization of angiogenesis in tumors,^[12] an important hallmark of cancer, as well as tissue responses to vascular-targeted therapies.^[14] High-resolution OA imaging at multiple wavelengths further provided new insights into tissue oxygenation and hypoxia in tumors^[79] as well as on the proliferation of genetically labeled cells.^[8] On the other hand, OA is gaining maturity as a neuroimaging tool.^[80] High-resolution imaging of cortical vascular networks can provide new insights into cerebrovascular function in health

and disease.^[20] Regarding potential clinical applications, OAM may provide new solutions to unmet clinical needs. A medical field that can particularly benefit from the new capabilities of OAM is dermatology.^[81] OAM can cover all layers composing the human skin and has been shown to represent a valuable tool to visualize psoriasis and eczema^[13] or burns and other wounds.^[82]

In conclusion, we expect that the suggested MB-OAM framework significantly enhances the performance of this modality and enable the visualization of previously unresolvable structures beyond the acoustic diffraction barrier. The forward model accurately accounts for the SIR of the transducer and the broadband nature of the induced pressure waves, which is essential for accurate reconstruction of OA images. The fact that this could be achieved with low memory requirements and in a relatively short time anticipates its general applicability as a biomedical research tool and can further boost the translation of OAM as a label-free angiographic imaging method in the clinical setting.

4. Experimental Section

Forward Modeling: Excitation of OA signals in OAM was achieved with nanosecond laser pulses fulfilling thermal and stress confinement conditions. In an acoustically uniform and non-attenuating medium, the time-resolved pressure signal $p(x, t)$ at a point x is given as a function of absorbed optical energy density distribution $H(x')$ as^[83]

$$p(x, t) = \frac{\Gamma}{4\pi c} \frac{\partial}{\partial t} \int_{S'(t)} \frac{H(x')}{|x - x'|} dS' \quad (1)$$

where Γ is the Grueneisen parameter, c is the speed of sound, x' is a point where light is absorbed, and $S'(t)$ is a spherical surface defined as $|x - x'| = ct$. The forward model in Equation (1) was discretized with a two-step procedure—the time derivative was discretized using the finite difference method, and the surface integral was discretized using trilinear interpolation of neighboring voxel values.^[35] Assuming a constant Γ and c , the discretized forward model is then expressed (in arbitrary units) as the linear system of equations

$$p = AH \quad (2)$$

where p is a vector of pressure signals at all scanning positions, A is the model matrix, and H is a vector of voxel values representing the absorbed energy density in the region of interest (ROI). The model matrix A describes the OA response to unit absorption at the voxel grid defined to cover the absorption distribution domain, and can be used to model the signals of a point detector with infinite bandwidth. More specifically, each column vector in A corresponds to one pair of voxel and scanning point. The OA signal collected by a finite-size transducer can be approximated by integrating pressure waves over the transducer surface.^[84] This approximation represents the SIR of the transducer, which can be modeled by dividing the transducer surface into sub-elements with position x_j and area Δx_j . The vector s of signals collected by the transducer at all scan positions is then expressed as

$$s = \sum_{j=1}^M p_{x_j} \Delta x_j \quad (3)$$

where M is the number of sub-elements covering the transducer surface (Figure 1c). Combining Equations (2) and (3), the discrete forward model becomes

$$s = \sum_{j=1}^M A_j \Delta x_j H = A_s H \quad (4)$$

Thereby, the model matrix A_s accounting for the SIR of the transducer is estimated as a weighted sum of M model matrices corresponding to M sub-elements.

Efficient Reconstruction Based on Scanning Symmetries: MB inversion involves minimizing an energy functional

$$H = \operatorname{argmin}_H \|s_m - A_s H\|_2^2 + \lambda R(H) \quad (5)$$

where s_m is the vector of measured signals, $R(H)$ is regularization term, and λ is the regularization parameter controlling the trade-off between regularization and data fidelity terms. The importance of $R(H)$ is twofold — it makes the optimization procedure more robust to noise, and it incorporates a priori knowledge of the image H . Herein, the standard Tikhonov regularization based on the L2 norm was considered, where $R(H)$ is given by

$$R(H) = \|H\|_2^2 \quad (6)$$

MB inversion with Tikhonov regularization as the MB-L2 method was referred. L1 regularization based on the L1 norm was also considered, where $R(H)$ is given by

$$R(H) = \|H\|_1 \quad (7)$$

MB inversion with L1 regularization as the MB-L1 method was referred. The solution to Equation (5) was computed iteratively with the LSQR algorithm^[85] for MB-L2, and with the FISTA algorithm^[86] for MB-L1.

In both LSQR and FISTA algorithms, the most computationally demanding operations are the matrix-vector multiplications $A_s u$ and $A_s^T v$, where u and v are updated in each iteration. The computational burden originates from the large-scale nature of OAM. This leads to a huge model matrix covering each pair of voxel and scanning position in the entire ROI, even if it is stored in sparse format.^[43] However, since the spherically focused transducer barely senses voxels sufficiently distant in the lateral direction, the corresponding model matrix values were approximated as 0, i.e., the model matrix only covers a 1 mm lateral extent (Figure 1d), independent of an arbitrarily large ROI. The depth extent of model matrix scales with the collected dataset. Also, given that the transducer sensitivity field is translational-symmetric, the model vector is equivalent if the relative position between voxel and scanning point is maintained. Therefore, it was sufficient to generate the model matrix for a single scanning position, as it includes all unique lateral distances between pairs of voxel and scanning point. The “compressed” model matrix can then be pre-calculated in a reasonable time and stored in a memory-efficient way. To perform the matrix-vector multiplications, translational symmetries were considered to find the correspondences between voxels and model vectors (Figure 1b). Specifically, two coordinate systems were maintained — an absolute coordinate system to index over the voxel grid, and a relative coordinate system, with the origin at each scanning position, to retrieve the corresponding model vector based on the lateral distance between a given voxel and the origin. The matrix-vector multiplications were parallelized and executed on GPU, which greatly improved computational speed.

Numerical Simulations: The performance of the MB-OAM methods, namely MB-L2 and MB-L1, was first tested on numerical simulations. In the first simulation, the absorption distribution within a $(2 \times 2 \times 3)$ mm³ FOV was modeled as four truncated paraboloids with diameters (60, 100, 150, and 200) μ m (Figure 1e), and a 25 μ m step size was used. The paraboloids were positioned 0.5 mm away from the center of the FOV in the lateral (x and y) directions, and equally separated within a ± 1 mm range from the acoustic focus in axial (z) direction. The transducer surface was divided into 1200 sub-elements and the raw OA signals at the center of each sub-element were calculated analytically.^[84] The temporal sampling frequency was set to 250 MHz for all simulations, consistent with the experimental setting. The OA signals were normalized to the maximum absolute value and 2% white Gaussian noise (standard deviation of 0.02) was added. MB-L2 and SAFT^[10] were used for image formation in this first simulation.

The second simulation was performed by considering two truncated paraboloids with 20 μm diameter at the axial location of the acoustic focus for a FOV of $(200 \times 200 \times 150) \mu\text{m}^3$ and 5 μm step size. The paraboloids were first separated by 60 μm in the x direction to ensure they can be resolved by all three methods in comparison — SAFT, MB-L2, and MB-L1 (Figure 2a, left). Subsequently, they were separated by 40 μm in the x direction, which was set to be the separation distance beyond the acoustic diffraction limit for the band-pass filters employed (Figure 2a, right). Specifically, the raw signals and the model matrix were band-pass filtered between 0.5 MHz and 80.0 MHz, yielding a diffraction-limited resolution of 61 μm .^[45] The OA signals were normalized by the maximum absolute value and no noise was added.

A third simulation was performed to validate the capability of MB-L1 to accurately quantify micro-vessel dimensions. To this end, OA signals corresponding to truncated paraboloid absorbers with diameters of (20, 30, 45, 60, 80, and 100) μm were simulated, and independently inverted with both MB-L2 and MB-L1. The simulated absorbers were positioned at the depth of the acoustic focus and at the center of a FOV of $(250 \times 250 \times 250) \mu\text{m}^3$ with 5 μm step size. The OA signals were normalized to the maximum absolute value and 2% white Gaussian noise was added.

A fourth simulation was performed to examine the effect of EIR on the reconstruction performance. OA signals corresponding to a truncated paraboloid absorber with 20 μm diameter placed at the acoustic focus in a FOV of $(200 \times 200 \times 200) \mu\text{m}^3$ were simulated at 5 μm step size. The OA signals were band-pass filtered in different frequency bands prior to reconstruction to simulate the EIR effect. Specifically, 5 different low cut-off frequencies were simulated, namely (1, 5, 10, 15, and 20) MHz. For each low cut-off frequency, 7 different high cut-off frequencies were simulated, namely (100, 85, 75, 60, 50, 40, and 25) MHz. This results in a total of 35 simulated detection bandwidths. Image reconstruction with the band-pass filtered OA signals was performed with the MB-L2 method, and FWHM values were extracted from the central profile of maximum intensity projection (MIP) images along the depth direction.

A fifth simulation was performed to confirm the super-resolution imaging capability of the MB-L1 method. For this, complex structures mimicking vascular networks with two different densities were simulated. Theoretical vessel-mimicking 2D images were placed at the acoustic focal plane in a $(1 \times 1 \times 0.2) \text{mm}^3$ FOV. The OA signals were simulated by considering the superposition of truncated paraboloid absorbers with 20 μm diameter at each voxel corresponding to the vascular structure. Image reconstruction was then performed with both MB-L2 and MB-L1 methods.

OAM Set-Up: A recently proposed burst-mode OAM system was used^[11] (Figure S1, Supporting Information). The system employs a custom-made, 9 μm foil PVDF spherically focused transducer (7 mm focal distance and 0.43 NA). Three laser sources at 532 nm, 578 nm, and 1064 nm were combined and coupled into a multimode fiber, which was guided through a central hole (0.9 mm diameter) of the transducer, thus providing concentric illumination and acoustic detection. Two of the laser sources have fixed wavelengths at 532 nm and 1064 nm (Onda 532 and 1064 nm, Bright Solutions, UK), and the third source is a tunable dye laser (Credo, Sirah Lasertechnik, Germany) with wavelength set to 578 nm. The transducer was translated laterally in the x - y plane above the sample (Figure 1a) to acquire a time-resolved OA signal at each scanning position. Specifically, a fast-moving scanning stage moves constantly forth and back between the boundaries of the previously defined scan window while monitoring its position. Following each pre-defined incremental stage movement, all three lasers were triggered in a cascade with a 6 μs delay in between. Motion artifacts were avoided by averting acceleration and deceleration at each scanning position. The system thus enables rapid acquisition of multi-wavelength volumetric datasets over large FOV. In all experiments, the temporal sampling frequency was set to 250 MHz and no signal averaging was performed.

Phantom Experiments: The MB-OAM framework was tested on two phantom experiments. A first phantom was used to test if MB-L1 is able to break the acoustic diffraction limit on experimental data. This consisted of a single micro-sphere with 20 μm diameter embedded in 1.3% (w/v) agar. The phantom was placed with the micro-sphere at the axial location of

the acoustic focus and a scan covering a $(200 \times 200 \times 150) \mu\text{m}^3$ was performed with 5 μm step size. The 532 nm laser source was used, with up to 2.5 kHz pulse repetition rate (PRR) and 50 μJ per-pulse energy (PPE). The single micro-sphere image in the phantom was first individually formed. Subsequently, the signal volume was artificially shifted by 40 μm in the x direction and super-imposed with the original volume, which is equivalent to the signal volume of two micro-spheres separated by the same distance.

A second phantom consisting of four carbon fibers with 7 μm diameter embedded in 1.3% (w/v) agar was imaged. The purpose of this phantom experiment was to assess the overall performance of SAFT and the MB-OAM framework to reconstruct elongated structures. The scan covered a $(1 \times 2 \times 1) \text{mm}^3$ FOV with 10 μm step size. The PRR was limited to 2.5 kHz and the PPE of the 532 nm laser was set to 50 μJ .

In Vivo Mouse Skin Imaging: The in vivo imaging performance of the MB-OAM framework was tested by imaging dorsal mouse skin. To this end, a CD-1 mouse (8 weeks old; Charles River Laboratories, Germany) was anesthetized with isoflurane, and placed in prone position on a heating pad. The back skin was shaved and cleaned before imaging. Vet ointment (Bepanthen, Bayer AG, Leverkusen, Germany) was applied on the eyes of the mice to prevent any dehydration during scanning and to protect them from laser light. Blood oxygen saturation, heart rate and body temperature were continuously monitored (PhysioSuite, Kent Scientific) and the temperature was maintained at $\sim 36^\circ\text{C}$ with a heating pad. A scan covering a $(10 \times 30) \text{mm}^2$ FOV with a 25 μm step size was performed, giving a volumetric dataset at each wavelength (532 nm, 578 nm, and 1064 nm). The PRR was limited to up to 2.5 kHz and the PPEs for the three lasers were set to 25 μJ , 25 μJ , and 100 μJ , respectively. Before reconstruction, the raw signals were band-pass filtered between 1 MHz and 100 MHz, and further median filtered with kernel size of $3 \times 3 \times 3$. The mouse was housed in a ventilated cage inside a temperature-controlled room under a 12-hour dark/light cycle. The animal experiment was performed in accordance with the Swiss Federal Act on Animal Protection and was approved by the Canton Veterinary Office Zurich.

Image Visualization and Vessel Quantification: Visualization of the dorsal skin vasculature was done using MIPs along all Cartesian dimensions. Volumetric rendering was performed in Paraview 5.8.0.^[87] The images of the mouse skin vasculature were shown with color-encoded depth. This was done by multiplying a background map (reconstructed volume), a foreground map (3-channel color encoder), and a transparency value. Foreground colors were set to blue, green, and orange from deeper to shallower regions. The number of vessels was quantified with a previously reported AVSA algorithm.^[55] In short, reconstructed images were binarized, skeletonized, and vessel center-lines fitted by a spline. Vessel edges were found by computing the image gradient along the normal direction of the central line. To quantify the number of vessels achieved in SAFT, MB-L2, and MB-L1, two signal volumes acquired at 532 nm and 578 nm from the multi-wavelength in vivo dataset were used. Each of the two volumes were further split into half along the y direction, which increases the sample size and gives a total of four individual datasets. Reconstructed vessels in an upper-right sub-region were individually visualized based on branch point, central line and edge (Figure 3e). The number of vessels in images reconstructed with SAFT, MB-L2 and MB-L1 was plotted, and the mean value was noted for all three methods (Figure 3f).

Optical Angiographic Imaging: The in vivo performance of the MB-OAM image formation framework was validated against wide-field optical imaging. To this end, the dorsal skin of CD-1 mouse (20 weeks old; Charles River Laboratories, Germany) was sequentially imaged with different modalities. The mouse was anesthetized with isoflurane (3% v/v for induction, 1.5% v/v for maintenance) in a mixture of air (0.8 L min^{-1}) and oxygen (0.2 L min^{-1}). The back skin was shaved and cleaned before imaging. Vet ointment (Bepanthen, Bayer AG, Leverkusen, Germany) was applied on the eyes of the mice to prevent any dehydration during scanning and to protect them from laser light. Blood oxygen saturation, heart rate and body temperature were continuously monitored (PhysioSuite, Kent Scientific) and the temperature was maintained at $\sim 36^\circ\text{C}$ with a heating pad. The mouse was placed in prone position on a heating pad maintaining body temperature during the experiment. First, a USB microscope (Dino-lite digital microscope, Taiwan) was used to take a bright field

image of the mouse. Subsequently, epi-fluorescence images were taken in the first and second near infrared windows (NIR-I and NIR-II). Imaging was performed after tail-vein injection of ICG (100 μ L, 1 mg mL⁻¹, Sigma-Aldrich Chemie GmbH, Switzerland). The fluorescence image was recorded with an EMCCD camera (iXon Life, Andor, UK) under 700 nm excitation. Time-lapse fluorescence images in the NIR-II were recorded with a commercial SWIR camera (WiDy SenS 640V-ST, NiT, France) under 855 nm excitation. An OAM image was also acquired at 532 nm excitation wavelength and 25 μ m step size, covering a FOV of (12 \times 6) mm². A big vertical vessel in the middle of the mouse back was selected as an anatomical landmark for comparison of the different modalities. All animal experiments were performed in accordance with the Swiss Federal Act on Animal Protection and were approved by the Canton Veterinary Office Zurich.

Human Skin Imaging: Nailfold imaging in three healthy volunteers was performed to demonstrate the general applicability of the MB-OAM framework in humans. All volunteers were informed and gave written consent to participate in the experiments. Dilation and constriction of the microvasculature in this region was achieved with a thermal stimulation protocol consisting of two main steps.^[88] First, the hand of the volunteer was immersed in cold water (~15 °C) for 5 min. Three consecutive scans of the index finger of this hand, each taking ~1.5 min, were performed immediately after immersion. Subsequently, the same hand was immersed in warm water (~40 °C) for 5 min and the scans were repeated immediately after. All scans were performed at 532 nm and 10 μ m step size, covering a (4 \times 3) mm² FOV. The PPE and the PRR of the laser were set to 25 μ J and 2 kHz, respectively. Images of the entire FOV were first reconstructed with MB-L2. To this end, OA signals were divided into different frequency bands.^[89] Specifically, band-pass filters with cut-off frequencies (10–20, 20–30, 30–40, and 40–60) MHz were applied. OA signals in each frequency band were independently used for reconstruction considering a regularization parameter of 1000 and 5 iterations. A weighted sum (weighting factors of 0.45, 0.4, 0.1, and 0.05 from low to high frequency bands) of the reconstructed images was then calculated. Images of a smaller FOV (1.6 \times 0.8) mm² at the junction of the nail and skin were formed with MB-L1. To this end, OA signals were band-pass filtered with cut-off frequencies 20 MHz – 25 MHz. Profiles corresponding to different microvessels were extracted from the 3D images to assess the dilation from cold to warm stimulus. The width of the corresponding vessels was estimated via Gaussian fitting of the profiles. Differences were assessed for different vessels of the same volunteer and across volunteers. The MB-L2 and MB-L1 images were visualized as MIPs along the z (depth) dimension, while the depth information was further color-encoded from orange to blue, corresponding to shallow and deep regions.

Wrist imaging in another healthy volunteer was performed to demonstrate the deep-tissue imaging capability of the MB-L2 and MB-L1 reconstruction methods. This volunteer was informed and gave written consent to participate in this experiment. A scan was performed at 532 nm and 1064 nm with 20 μ m step size covering a (6 \times 6) mm² FOV. The PPE and the PRR of the laser were set to 25 μ J and 2 kHz, respectively.

Supporting Information

Supporting Information is available from the Wiley Online Library or from the author.

Acknowledgements

This work was supported by the Helmut Horten Stiftung (Project Deep Skin, X.L.D.B.) and by the European Research Council under grant agreement ERC-2015-CoG-682379 (D.R.). The development of the ultrawideband ultrasonic detector was supported by the grant from the Russian Science Foundation (project 19-75-10055, P.S.).

Open access funding provided by Universitat Zurich.

Conflict of Interest

The authors declare no conflict of interest.

Author Contributions

W.L. and U.A.T.H. contributed equally to this work. X.L.D.B. and D.R. conceived the concept and devised the study. W.L., U.H., A.O., Y.G., and X.L.D.B. developed the reconstruction framework and implemented the reconstruction code. U.H. developed the imaging system. U.H. and W.L. performed all experiments. W.L. and U.H. performed the reconstructions and data analysis. Q.Z. and Z.C. performed the optical imaging experiments. J.R. implemented depth-encoding visualization and vessel quantification code. D.R. and X.L.D.B. supervised the work. All authors contributed to writing and revising the manuscript.

Data Availability Statement

The data that support the findings of this study are available from the corresponding author upon reasonable request.

Keywords

intravital microscopy, model-based image reconstruction, skin imaging, super-resolution

Received: July 13, 2021

Revised: March 4, 2022

Published online: April 3, 2022

- [1] L. V. Wang, J. Yao, *Nat. Methods* **2016**, *13*, 627.
- [2] X. L. Deán-Ben, S. Gottschalk, B. Mc Larney, S. Shoham, D. Razansky, *Chem. Soc. Rev.* **2017**, *46*, 2158.
- [3] A. Taruttis, V. Ntziachristos, *Nat. Photonics* **2015**, *9*, 219.
- [4] L. Li, L. Zhu, C. Ma, L. Lin, J. Yao, L. Wang, K. Maslov, R. Zhang, W. Chen, J. Shi, L. V. Wang, *Nat. Biomed. Eng.* **2017**, *1*, 71.
- [5] X. L. Deán-Ben, T. F. Fehm, S. J. Ford, S. Gottschalk, D. Razansky, *Light: Sci. Appl.* **2017**, *6*, e16247.
- [6] X. L. Deán-Ben, H. López-Schier, D. Razansky, *Sci. Rep.* **2017**, *7*, 6850.
- [7] H. F. Zhang, K. Maslov, G. Stoica, L. V. Wang, *Nat. Biotechnol.* **2006**, *24*, 848.
- [8] A. P. Jathoul, J. Laufer, O. Ogunlade, B. Treeby, B. Cox, E. Zhang, P. Johnson, A. R. Pizzey, B. Philip, T. Marafioti, M. F. Lythgoe, R. B. Pedley, M. A. Pule, P. Beard, *Nat. Photonics* **2015**, *9*, 239.
- [9] J. Kim, J. Y. Kim, S. Jeon, J. W. Baik, S. H. Cho, C. Kim, *Light: Sci. Appl.* **2019**, *8*, 103.
- [10] S. Park, C. Lee, J. Kim, C. Kim, *Biomed. Eng. Lett.* **2014**, *4*, 213.
- [11] U. A. T. Hofmann, J. Rebling, H. Estrada, P. Subochev, D. Razansky, *Opt. Lett.* **2020**, *45*, 2522.
- [12] M. Omar, M. Schwarz, D. Soliman, P. Symvoulidis, V. Ntziachristos, *Neoplasia* **2015**, *17*, 208.
- [13] J. Aguirre, M. Schwarz, N. Garzorz, M. Omar, A. Buehler, K. Eyerich, V. Ntziachristos, *Nat. Biomed. Eng.* **2017**, *1*, 68.
- [14] K. Haedicke, L. Agemy, M. Omar, A. Berezhnoi, S. Roberts, C. Longo-Machado, M. Skubal, K. Nagar, H. Hsu, K. Kim, T. Reiner, J. Coleman, V. Ntziachristos, A. Scherz, J. Grimm, *Nat. Biomed. Eng.* **2020**, *4*, 286.
- [15] I. Stoffels, S. Morscher, I. Helfrich, U. Hillen, J. Leyh, N. C. Burton, T. C. P. Sardella, J. Clausen, T. D. Poeppel, H. S. Bachmann, A. Roesch, K. Griewank, D. Schadendorf, M. Gunzer, J. Klode, *Sci. Transl. Med.* **2015**, *7*, 317ra199.
- [16] I. Ivankovic, E. Merčep, C. Schmedt, X. L. Deán-Ben, D. Razansky, *Radiology* **2019**, *291*, 45.
- [17] M. Jeon, J. Kim, C. Kim, *Med. Biol. Eng. Comput.* **2016**, *54*, 283.
- [18] X. Li, U. S. Dinish, J. Aguirre, R. Bi, K. Dev, A. B. E. Attia, S. Nitkunanarajah, Q. H. Lim, M. Schwarz, Y. W. Yew, S. T. G. Thng, V. Ntziachristos, M. Olivo, *J. Biophotonics* **2019**, *12*, 201800442.

- [19] H. Estrada, J. Turner, M. Kneipp, D. Razansky, *Laser Phys. Lett.* **2014**, *11*, 045601.
- [20] J. Rebling, H. Estrada, S. Gottschalk, G. Sela, M. Zwack, G. Wissmeyer, V. Ntziachristos, D. Razansky, *J. Biophotonics* **2018**, *11*, 201800057.
- [21] W. Liu, D. M. Shcherbakova, N. Kurupassery, Y. Li, Q. Zhou, V. V. Verkhusha, J. Yao, *Sci. Rep.* **2018**, *8*, 11123.
- [22] M. Li, H. F. Zhang, K. Maslov, G. Stoica, L. V. Wang, *Opt. Lett.* **2006**, *31*, 474.
- [23] T. Stepinski, F. Lingvall, *8th Eur. Conf. Synth. Aperture Radar*, VDE, Aachen, Germany **2010**, p. 1.
- [24] J. Turner, H. Estrada, M. Kneipp, D. Razansky, *Optica* **2017**, *4*, 770.
- [25] F. Spadin, M. Jaeger, R. Nuster, P. Subochev, M. Frenz, *Photoacoustics* **2020**, *17*, 100149.
- [26] J. Park, S. Jeon, J. Meng, L. Song, J. S. Lee, C. Kim, *J. Biomed. Opt.* **2016**, *21*, 036010.
- [27] M. Mozaffarzadeh, M. H. H. Varnosfaderani, A. Sharma, M. Pramanik, N. Jong, M. D. Verweij, *J. Biophotonics* **2019**, *12*, 201900133.
- [28] M. Xu, L. V. Wang, *Phys. Rev. E* **2005**, *71*, 016706.
- [29] B. E. Treeby, B. T. Cox, *J. Biomed. Opt.* **2010**, *15*, 021314.
- [30] H. Jin, R. Zhang, S. Liu, Y. Zheng, *IEEE Trans. Med. Imaging* **2019**, *38*, 2926.
- [31] J. Aguirre, A. Giannoula, T. Minagawa, L. Funk, P. Turon, T. Durduran, *Biomed. Opt. Express* **2013**, *4*, 2813.
- [32] L. Yao, L. Xi, H. Jiang, *Sci. Rep.* **2015**, *4*, 4960.
- [33] X. L. Deán-Ben, H. Estrada, M. Kneipp, J. Turner, D. Razansky, *Photons Plus Ultrasound Imaging Sens.* **2014**, *8943*, 8943V.
- [34] K. Mitsuhashi, K. Wang, M. A. Anastasio, *Photoacoustics* **2014**, *2*, 21.
- [35] L. Ding, X. L. Deán-Ben, D. Razansky, *IEEE Trans. Med. Imaging* **2017**, *36*, 1858.
- [36] G. Drozdov, A. Levi, A. Rosenthal, *IEEE Trans. Med. Imaging* **2019**, *38*, 2326.
- [37] S. Arridge, P. Beard, M. Betcke, B. Cox, N. Huynh, F. Lucka, O. Ogundade, E. Zhang, *Phys. Med. Biol.* **2016**, *61*, 8908.
- [38] J. Friel, M. Haltmeier, *Inverse Probl.* **2018**, *34*, 024006.
- [39] L. Ding, X. L. Deán-Ben, N. C. Burton, R. W. Sobol, V. Ntziachristos, D. Razansky, *IEEE Trans. Med. Imaging* **2017**, *36*, 1676.
- [40] A. Hauptmann, F. Lucka, M. Betcke, N. Huynh, J. Adler, B. Cox, P. Beard, S. Ourselin, S. Arridge, *IEEE Trans. Med. Imaging* **2018**, *37*, 1382.
- [41] T. P. Matthews, J. Poudel, L. Li, L. V. Wang, M. A. Anastasio, *SIAM J. Imaging Sci.* **2018**, *11*, 1560.
- [42] A. Özbek, X. L. Deán-Ben, D. Razansky, *Optica* **2018**, *5*, 857.
- [43] L. Ding, D. Razansky, X. L. Deán-Ben, *IEEE Trans. Med. Imaging* **2020**, *39*, 2931.
- [44] T. Shan, J. Qi, M. Jiang, H. Jiang, *Appl. Opt.* **2017**, *56*, 4426.
- [45] J. Yao, L. V. Wang, *Laser Photonics Rev.* **2013**, *7*, 758.
- [46] A. Rosenthal, V. Ntziachristos, D. Razansky, *Curr. Med. Imaging Rev.* **2013**, *9*, 318.
- [47] P. C. Hansen, *Fundam. Algorithms, Society for Industrial and Applied Mathematics, Society for Industrial and Applied Mathematics* **2010**.
- [48] N. Davoudi, X. L. Deán-Ben, D. Razansky, *Nat. Mach. Intell.* **2019**, *1*, 453.
- [49] S. R. Arridge, M. M. Betcke, B. T. Cox, F. Lucka, B. E. Treeby, *Inverse Probl.* **2016**, *32*, 115012.
- [50] S. Farsiu, M. D. Robinson, M. Elad, P. Milanfar, *IEEE Trans. Image Process.* **2004**, *13*, 1327.
- [51] S. Mallat, G. Yu, *IEEE Trans. Image Process.* **2010**, *19*, 2889.
- [52] J. Yang, J. Wright, T. S. Huang, Y. Ma, *IEEE Trans. Image Process.* **2010**, *19*, 2861.
- [53] Y. Wang, J. Qiao, J. Li, P. Fu, S. Chu, J. F. Roddick, *Measurement* **2014**, *47*, 946.
- [54] A. Oyama, S. Kumagai, N. Arai, T. Takata, Y. Saikawa, K. Shiraishi, T. Kobayashi, J. Kotoku, *J. Radiat. Res.* **2018**, *59*, 501.
- [55] H. Estrada, J. Rebling, W. Sievert, D. Hladik, U. Hofmann, S. Gottschalk, S. Tapio, G. Multhoff, D. Razansky, *Bone* **2020**, *133*, 115251.
- [56] C. Lutzweiler, X. L. Deán-Ben, D. Razansky, *Med. Phys.* **2014**, *41*, 013302.
- [57] Y. Lou, S. Park, F. Anis, R. Su, A. A. Oraevsky, M. A. Anastasio, *IEEE Trans. Comput. Imaging* **2019**, *5*, 437.
- [58] Y. Han, L. Ding, X. L. Deán Ben, D. Razansky, J. Prakash, V. Ntziachristos, *Opt. Lett.* **2017**, *42*, 979.
- [59] X. L. Deán-Ben, G. A. Pang, F. M. Espinosa, D. Razansky, *Appl. Phys. Lett.* **2015**, *107*, 051105.
- [60] H. Ma, K. Xiong, J. Wu, X. Ji, S. Yang, *Appl. Phys. Lett.* **2019**, *114*, 133701.
- [61] M. Seeger, D. Soliman, J. Aguirre, G. Diot, J. Wierzbowski, V. Ntziachristos, *Nat. Commun.* **2020**, *11*, 2910.
- [62] S. Bu, Z. Liu, T. Shiina, K. Kondo, M. Yamakawa, K. Fukutani, Y. Sameda, Y. Asao, *IEEE Trans. Biomed. Eng.* **2012**, *59*, 1354.
- [63] F. M. Brochu, J. Brunker, J. Joseph, M. R. Tomaszewski, S. Morscher, S. E. Bohndiek, *IEEE Trans. Med. Imaging* **2017**, *36*, 322.
- [64] E. Abbe, *Arch. Mikrosk. Anat.* **1873**, *9*, 413.
- [65] Y. M. Sigal, R. Zhou, X. Zhuang, *Science* **2018**, *361*, 880.
- [66] S. Vilov, B. Arnal, E. Bossy, *Opt. Lett.* **2017**, *42*, 4379.
- [67] X. L. Deán-Ben, D. Razansky, *Light: Sci. Appl.* **2018**, *7*, 18004.
- [68] P. Zhang, L. Li, L. Lin, J. Shi, L. V. Wang, *Light: Sci. Appl.* **2019**, *8*, 36.
- [69] X. L. Deán-Ben, J. Robin, R. Ni, D. Razansky, (Preprint) *arXiv:2007.00372*, unpublished, July **2020**.
- [70] X. Li, Y. Hu, X. Gao, D. Tao, B. Ning, *Signal Process.* **2010**, *90*, 405.
- [71] G. Chaudhary, M. Roumeliotis, J. J. L. Carson, M. A. Anastasio, *Proc. SPIE* **2010**, *7564*, 756434.
- [72] J. Prakash, S. K. Kalva, M. Pramanik, P. K. Yalavarthy, *J. Biomed. Opt.* **2021**, *26*, 086004.
- [73] B. Pan, S. R. Arridge, F. Lucka, B. T. Cox, N. Huynh, P. C. Beard, E. Z. Zhang, M. M. Betcke, *IEEE Trans. Comput. Imaging* **2021**, *7*, 879.
- [74] Y. Li, L. Li, L. Zhu, K. Maslov, J. Shi, P. Hu, E. Bo, J. Yao, J. Liang, L. Wang, L. V. Wang, *Nat. Photonics* **2020**, *14*, 164.
- [75] S. Biton, N. Arbel, G. Drozdov, G. Gilboa, A. Rosenthal, *IEEE Trans. Med. Imaging* **2019**, *16*, 100142.
- [76] D. M. Ego, R. K. W. Chee, R. J. Zemp, *Opt. Lett.* **2018**, *43*, 2221.
- [77] X. L. Deán-Ben, A. Özbek, H. López-Schier, D. Razansky, *Phys. Rev. Lett.* **2019**, *123*, 174301.
- [78] M. Omar, J. Aguirre, V. Ntziachristos, *Nat. Biomed. Eng.* **2019**, *3*, 354.
- [79] A. Ron, X. L. Deán-Ben, S. Gottschalk, D. Razansky, *Cancer Res.* **2019**, *79*, 4767.
- [80] S. Bodea, G. G. Westmeyer, *Front. Neurosci.* **2021**, *15*, 333.
- [81] X. L. Deán-Ben, D. Razansky, *Exp. Dermatol.* **2021**, *30*, 1598.
- [82] D. Li, L. Humayun, E. Vienneau, T. Vu, J. Yao, *JID Innov.* **2021**, *1*, 100039.
- [83] B. T. Cox, S. Kara, S. R. Arridge, P. C. Beard, *J. Acoust. Soc. Am.* **2007**, *121*, 3453.
- [84] D. Queirós, X. L. Deán-Ben, A. Buehler, D. Razansky, A. Rosenthal, V. Ntziachristos, *J. Biomed. Opt.* **2013**, *18*, 076014.
- [85] C. C. Paige, M. A. Saunders, *ACM Trans. Math. Softw.* **1982**, *8*, 43.
- [86] A. Beck, M. Teboulle, *SIAM J. Imaging Sci.* **2009**, *2*, 183.
- [87] U. Ayachit, *The ParaView Guide: A Parallel Visualization Application*, Kitware, Clifton Park, NY **2015**.
- [88] A. A. Plumb, N. T. Huynh, J. Guggenheim, E. Zhang, P. Beard, *Eur. Radiol.* **2018**, *28*, 1037.
- [89] J. Aguirre, B. Hindelang, A. Bereznoi, U. Darsow, F. Lauffer, K. Eyering, T. Biedermann, V. Ntziachristos, *Photoacoustics* **2018**, *10*, 31.